Droplet spreading on chemically heterogeneous substrates

Rajagopal Vellingiri, Nikos Savva, and Serafim Kalliadasis
Department of Chemical Engineering, Imperial College London, London SW7 2AZ, United Kingdom
(Received 16 February 2011; published 9 September 2011)

Consider the spreading dynamics of a two-dimensional droplet over chemically heterogeneous substrates. Assuming small slopes and strong surface tension effects, a long-wave expansion of the Stokes equations yields a single evolution equation for the droplet thickness. The contact line singularity is removed by assuming slip at the liquid-solid interface. The chemical nature of the substrate is incorporated by local variations in the microscopic contact angle, which appear as boundary conditions in the governing equation. By asymptotically matching the flow in the bulk of the droplet with the flow in the vicinity of the contact lines, we obtain a set of coupled ordinary differential equations for the locations of the two droplet fronts. We verify the validity of our matching procedure by comparing the solutions of the ordinary differential equations with solutions of the full governing equation. The droplet dynamics is examined in detail via a phase-plane analysis. A number of interesting features that are not present in chemically homogeneous substrates are found, such as the existence of multiple equilibria, the pinning of the droplet fronts at localized chemical features, and the possibility for the droplet fronts to exhibit a stick-slip behavior.

DOI: 10.1103/PhysRevE.84.036305 PACS number(s): 47.55.D−, 68.15.+e, 68.08.Bc, 47.55.nd

I. INTRODUCTION

Wetting phenomena occur in a wide variety of natural phenomena and technological applications, from the repellency of rain water droplets by certain plant leafs and insects walking on water, to oil recovery, inkjet printing, and more recent applications such as microfluidic devices. As a consequence, wetting, and particularly its utilization to manipulate droplet behavior, has been an active topic of both theoretical and experimental research for several decades [1–4].

One of the most extensively studied topics in wetting is the spreading of liquid droplets on ideally homogeneous solid substrates [5–10]. Oftentimes, substrates are not ideally homogeneous but they are characterized by topographical defects or variations which can cause substantial changes to the spreading dynamics; e.g., they can pin the droplet fronts at localized features, induce stick-slip behavior and hysteresis, or cause the droplet to move in a preferred direction. Recent studies of spreading on topographical substrates, either structured or random, both theoretical (e.g., [11–14]) and experimental (e.g., [15,16]), demonstrated many of these effects. Noteworthy is that current technological advances allow control of topographical features down to microscopic scales (e.g., [17,18]). The droplet spreading dynamics is also significantly influenced by the presence of additional effects and complexities, such as thermocapillarity (e.g., [10]), evaporation (e.g., [19]), or electric fields (e.g., [20]).

Of equal importance are the effects of chemical heterogeneities on the spreading dynamics. One of the first studies that examined droplet equilibria on flat chemically heterogeneous substrates was that by Cassie [21]. By using energetic and thermodynamic arguments, he obtained an effective contact angle θ_C that accounts for the areas occupied by different substrate chemistries. For example, when the substrate consists of only two different materials, he showed that

$$\cos\theta_C = \beta\cos\alpha_{s,1} + (1-\beta)\cos\alpha_{s,2}, \qquad (1)$$

where β is the area fraction of material 1 and $\alpha_{s,1}$, $\alpha_{s,2}$ are the equilibrium contact angles on substrates made of materials 1 and 2, respectively. The general applicability of Eq. (1) has been recently the subject of a vigorous debate [22–27]. It is generally accepted that this expression holds in an "averaged sense" [28] and cannot describe quantitatively all possible cases (after all, it is based on thermodynamics solely without any fluid dynamics). Indeed, a number of studies (e.g., [29–32]) with chemically heterogeneous substrates have demonstrated that the agreement of Eq. (1) with experiments is only qualitative.

Experimental studies with chemically heterogeneous substrates also observe that the droplet fronts tend to pin on localized chemical defects—much like the topographical substrates case mentioned earlier—as shown for instance in the work of Cubaud and Fermigier [33]. Another commonly reported feature of chemically heterogeneous substrates is that of a preferential droplet motion in the presence of favorable wettability gradients (e.g., [34,35]). If these are sufficiently strong, they can even move a droplet against gravity on an inclined plane [34]. More recent experimental studies examined spreading over striped chemical substrates (e.g., [36–38]). They reported preferential spreading along the substrate stripes and they also identified the possibility of pinning a sufficiently small droplet along a stripe as well as of stick-slip behavior for strong wettability contrasts between the heterogeneities.

At the theoretical front, several studies have examined wetting of chemically heterogeneous substrates. The early study by Greenspan [39] examined the effects of a wettability gradient on the motion of a three-dimensional viscous droplet by imposing a spatial variation on the equilibrium contact angle. The equation for the droplet motion was obtained from the long-wave limit of the Stokes regime and a slip model was utilized to remove the stress singularity associated with a moving contact line [40]. Greenspan also prescribed an empirical law that relates the contact line speed with the apparent contact angle. Other studies resorted to thermodynamic and energetic arguments and/or postulated equations. For example, the study

by Joanny and de Gennes [41] considered weak, localized chemical defects, using force balance equations along the contact line (but the weak heterogeneity limit precludes the possibility of contact angle hysteresis). Brochard [42] also employed force balance and energy arguments to deduce the wetting characteristics of a two-dimensional droplet in terms of the spreading coefficient along the substrate [42]. The work of Moulinet *et al.* [43] investigated the contact line dynamics on chemically heterogeneous substrates via postulated equations and under the assumption that it exhibits similar features with avalanche dynamics, but their theoretical results failed to agree with their experiments.

Schwartz and Eley [44] examined the motion of a three-dimensional droplet on chemically heterogenous substrates by utilizing the long-wave limit of the Stokes regime and by taking the equilibrium contact angle to be a prescribed function of position on the substrate as Greenspan did. However, instead of slip, a constant-thickness precursor film model was utilized to remove the stress singularity at the moving contact lines. The precursor film was obtained from the balance of the attractive and repulsive intermolecular forces of the disjoining pressure model these authors adopted. Thiele and Knobloch [45] used a similar precursor film model and focused on two-dimensional droplet spreading. The wettability defects were modeled by introducing variations in the attractive part of the disjoining pressure. They demonstrated that it is possible for an advancing front to get pinned at less hydrophilic regions and for a receding front to get pinned at more hydrophilic ones, obtaining also the various depinning transitions in the presence of imposed driving forces, such as body forces or temperature gradients. Other studies utilized the Lattice-Boltzmann method to perform simulations of spreading of nanodroplets on specific wettability configurations. For example, Huang *et al.* [46] investigated conditions under which alternating high and low wettability regions can induce a unidirectional motion [46], whereas Kusumaataja *et al.* performed computations on substrates with stripped regions of different equilibrium contact lines [47].

In the present study we perform a detailed and systematic investigation of two-dimensional droplet spreading over flat but chemically heterogeneous substrates with the aim to elucidate qualitatively the effects of substrate chemistry on wetting. Like some of the previous studies (e.g., [11,39,48,49]), we invoke the long-wave expansion of the Stokes equations and we remove the stress singularity associated with a moving contact line by using a slip model. Contrary to previous studies on chemical heterogeneities, we reduce the nonlinear free boundary value problem to a system of ordinary differential equations (ODEs) for the two moving fronts, which is a considerably simpler problem to solve numerically. More importantly, one of the novel aspects of this methodology is that it facilitates the extraction of generic equilibrium and dynamic features via a phase plane analysis which would not have been possible by a direct numerical treatment of the long-wave model.

The model and appropriate boundary conditions together with their nondimensionalization are outlined in Sec. II, by assuming that the chemical variations of the substrate occur at length scales that are much longer than the slip length. In Sec. III, the problem is analyzed via matched asymptotics which lead to a set of ODEs for the evolution of the two droplet fronts. The analysis builds on the singular perturbation methodology developed by Hocking [49] and by Savva and Kalliadasis [11] for droplet spreading over ideally homogeneous and topographical substrates, respectively. It is valid in the limit $\mathrm{Ca} \ll 1$, where Ca is the capillary number, defined as

$$\mathrm{Ca} = \frac{\mu U}{\sigma}, \tag{2}$$

where σ is the surface tension, μ is the liquid viscosity, and U is the (time dependent) fluid velocity. Not only is this a realistic assumption as many spreading experiments fall within the low-capillary-number regime, but it allows us to treat the droplet motion as a quasistatic one which in turn allows for analytical progress. Like Greenspan [39], the quasistatic assumption has also been invoked by Glasner [50], who obtained three-dimensional droplet profiles via a boundary integral formulation, but had nevertheless imposed the contact line velocity as a function of the apparent contact angle.

In Sec. IV A we offer comparisons of the numerical solution of the full partial differential equation (PDE) and the equations obtained by asymptotic matching. We also consider in detail the effects of slip and we demonstrate the possibility of a stick slip behavior as well as a hysteresis-like effect induced by the chemical heterogeneities. In Sec. IV B, we present a detailed investigation of the phase portrait of the two contact lines. We also determine the conditions under which two localized heterogeneities can trap a spreading droplet and the effects of having substrates with alternating regions with different wetting characteristics. Finally, our results are summarized in Sec. V.

II. PROBLEM FORMULATION

We consider a two-dimensional droplet that spreads on a flat, horizontal, and chemically heterogeneous substrate. The droplet cross section lies on the X-Z plane and has thickness $H(X,T)$ at time T. By neglecting gravitational effects and assuming that the free-surface slope is everywhere small, a long-wave expansion of the Stokes equations yields the following equation for the evolution of the droplet thickness:

$$\frac{\partial H}{\partial T} + \frac{\sigma}{3\mu}\frac{\partial}{\partial X}\left[H^2(H+3\Lambda)\frac{\partial^3 H}{\partial X^3}\right] = 0, \tag{3}$$

where μ and σ are the dynamic viscosity and surface tension of the fluid, respectively. Λ is the slip length associated with the Navier slip condition along the substrate,

$$U|_{Z=0} = \Lambda \left.\frac{\partial U}{\partial Z}\right|_{Z=0},$$

where $U(X,T)$ is the fluid velocity in the X direction. Even though there is some debate on the slip lengths reported in experimental studies, it is generally accepted that the slip lengths for hydrophilic substrates are typically of the order of nanometers and tend to be smaller compared to those for hydrophobic substrates (see, e.g., [51–53]).

Here, we assume that Λ is constant along the substrate. Admittedly, the slip length may exhibit local variations due to the chemical heterogeneities of the substrate, but provided

that such variations are not strong and do not alter the order of magnitude of the slip length, they are not expected to significantly alter the droplet behavior qualitatively, as we shall also demonstrate with numerical experiments later. Noteworthy is that keeping Λ constant is equivalent to keeping the thickness of the precursor film constant in a precursor film model (e.g., [54–56]), an assumption that has been invoked in previous studies on droplet spreading on chemically heterogeneous substrates with a precursor film model (e.g., [44]). In our model the chemical heterogeneities enter the problem by prescribing a locally varying microscopic contact angle at the contact points. Equation (3) is subject to contact angle conditions at the two moving fronts, zero-thickness conditions there, and the requirement that the droplet area remain constant at all times. The governing equation is made nondimensional by introducing the variables

$$x = \frac{X}{L}, \quad t = \frac{\sigma \tan^3 \alpha_s}{3\mu L} T,$$
$$h = \frac{H}{L \tan \alpha_s}, \quad \lambda = \frac{3L}{\Lambda \tan \alpha_s},$$

where α_s is some reference contact angle and L is the characteristic length scale associated with the cross-sectional area of the droplet, A, written as

$$L = \sqrt{\frac{A}{2 \tan \alpha_s}}.$$

For periodically structured substrates, α_s is typically taken to be the average contact angle, whereas for substrates with localized features it is taken to be the contact angle in a defect-free region of the substrate. In nondimensional variables, Eq. (3) becomes

$$\frac{\partial h}{\partial t} + \frac{\partial}{\partial x}\left[h^2(h+\lambda)\frac{\partial^3 h}{\partial x^3}\right] = 0. \tag{4}$$

Assuming that the left and right droplet fronts are located at $x = b(t)$ and $x = a(t)$, respectively (see Fig. 1), the boundary conditions outlined above become

$$h = 0 \quad \text{at} \quad x = a(t) \quad \text{and} \quad x = b(t), \tag{5a}$$
$$\frac{\partial h}{\partial x} = -g(a) \quad \text{at} \quad x = a(t), \tag{5b}$$
$$\frac{\partial h}{\partial x} = g(b) \quad \text{at} \quad x = b(t), \tag{5c}$$

together with the area constraint:

$$\int_b^a h\, dx = 2. \tag{5d}$$

Here $g(x)$ is an imposed function of x for the local variations of the microscopic contact angle, which characterizes a chemically heterogeneous substrate. In general, there is no restriction on the form of $g(x)$, apart from requiring that it be $O(1)$, that its derivatives be continuous, and that its variations occur at length scales that are much longer than the slip length, λ. As with related studies employing a slip condition (see, e.g., [11,49]), we anticipate sharp boundary layers in the vicinity of the moving fronts, where the slope of the free surface changes abruptly from the microscopic contact angle to an apparent contact angle in the bulk. As a consequence, an asymptotic analysis may be appropriately employed to deduce equations for the two moving fronts.

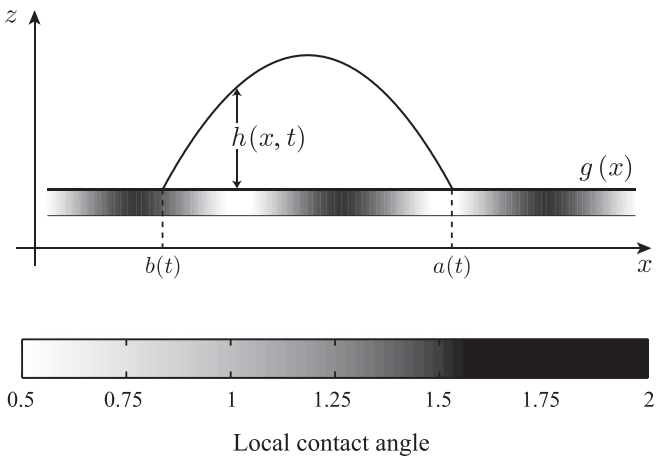

FIG. 1. Two-dimensional droplet spreading on a chemically heterogeneous substrate. In nondimensional units, the droplet thickness is given by $h(x,t)$, with its contact points located at $x = a(t)$ and $x = b(t)$. The local contact angle variations along the substrate are prescribed by $g(x)$. The substrate is shaded according to the color bar, which shows the range of $g(x)$ used throughout the present study.

III. MATCHED ASYMPTOTICS

To proceed, we restrict our attention to the regime $\mathrm{Ca} \ll 1$, which is equivalent to assuming that $|\dot{a}| = |da/dt| \ll 1$ and $|\dot{b}| = |db/dt| \ll 1$ in dimensionless units. In the bulk of the droplet, which we call the *outer region*, the motion is dominated by capillarity, whereas near the contact lines, in the *inner regions*, slip is predominant. By considering the dynamics in these disparate length scales and matching asymptotically their corresponding behaviors we shall obtain expressions for the spreading rates, $\dot{a}$ and $\dot{b}$.

A. Outer region

Away from the contact lines, slip is negligible. Hence, in the outer region, Eq. (4) simplifies to

$$\frac{\partial h}{\partial t} + \frac{\partial}{\partial x}\left[h^3\frac{\partial^3 h}{\partial x^3}\right] = 0. \tag{6}$$

Since the slope conditions depend on the details of the flow field in the vicinity of the contact lines, the solution to Eq. (6) in the outer region is to be determined subject to Eqs. (5a) and (5d). Treating $\dot{a}$ and $\dot{b}$ as the small parameters of the problem, we introduce a quasistatic expansion of the form

$$h(x,t) = h_0(x,a,b) + \dot{a}h_1(x,a,b) + \dot{b}h_2(x,a,b) + \cdots. \tag{7}$$

Our task is to find the asymptotic behavior of $h(x,t)$, as the contact points, $x = a(t)$ and $x = b(t)$, are approached. To $O(\dot{a}^0, \dot{b}^0)$, we obtain the following equation for h_0:

$$\frac{\partial^3 h_0}{\partial x^3} = 0. \tag{8}$$

Using then Eqs. (5a) and (5d) the solution to Eq. (8) is simply the parabolic profile

$$h_0 = \frac{\phi}{(a-b)}(a-x)(x-b), \tag{9}$$

where

$$\phi = \mp \partial h_0/\partial x|_{x=a(t),\,b(t)} = 12/(a-b)^2 \tag{10}$$

is the apparent contact angle, which, like $g(x)$, is $O(1)$, as required by the chosen scales of our nondimensionalization. To consider the next-order terms, take $\partial h_0/\partial t = \dot{a}\,\partial h_0/\partial a + \dot{b}\,\partial h_0/\partial b$. From the $O(\dot{a},\dot{b})$ terms, we obtain

$$\frac{\partial^3 h_1}{\partial x^3} = \frac{a-b}{\phi^2(a-x)^2(x-b)}, \tag{11a}$$

$$\frac{\partial^3 h_2}{\partial x^3} = \frac{a-b}{\phi^2(a-x)(b-x)^2}, \tag{11b}$$

for h_1 and h_2, respectively. Both differential equations are to be solved subject to homogeneous boundary conditions, namely

$$h_1 = h_2 = 0 \quad \text{at} \quad x = a(t), b(t), \tag{12a}$$

$$\int_b^a h_1\,dx = \int_b^a h_2\,dx = 0. \tag{12b}$$

Determining h_1 and h_2 is trivial; we successively integrate Eqs. (11a) and (11b), respectively, and apply the corresponding conditions in Eqs. (12a) and (12b). However, we are interested in the leading-order behavior of their slopes as $x \to a$ and $x \to b$. Hence, we have that

$$\frac{\partial h_1}{\partial x} \sim \begin{cases} -\dfrac{1}{\phi^2}\ln\left(e^2\dfrac{a-x}{a-b}\right), & \text{as } x \to a(t), \\ \dfrac{1}{\phi^2}, & \text{as } x \to b(t), \end{cases} \tag{13a}$$

$$\frac{\partial h_2}{\partial x} \sim \begin{cases} \dfrac{1}{\phi^2}, & \text{as } x \to a(t), \\ -\dfrac{1}{\phi^2}\ln\left(e^2\dfrac{x-b}{a-b}\right), & \text{as } x \to b(t), \end{cases} \tag{13b}$$

where $e = \exp(1)$. The neglected terms are $O(\eta\ln\eta)$, where $\eta = x-b$, when $x \to b(t)$ or $\eta = a-x$, when $x \to a(t)$. The idea is to match the slope of the outer solution with the inner one. By combining Eq. (9) with Eqs. (13a) and (13b), we obtain the leading-order slope of the outer solution as the contact points are approached:

$$-\frac{\partial h}{\partial x} \sim \phi + \frac{\dot{a}}{\phi^2}\ln\left(e^2\frac{a-x}{a-b}\right) - \frac{\dot{b}}{\phi^2}, \text{ as } x \to a(t), \tag{14}$$

$$\frac{\partial h}{\partial x} \sim \phi - \frac{\dot{b}}{\phi^2}\ln\left(e^2\frac{x-b}{a-b}\right) + \frac{\dot{a}}{\phi^2}, \text{ as } x \to b(t). \tag{15}$$

The above asymptotic expansions will be utilized in the matching with their corresponding asymptotic expansions from the inner regions. The matching will be carried out within some overlap regions such that ϕ is the dominant term in Eqs. (14) and (15), and the x-dependent logarithmic terms are the next-order corrections in their asymptotic expansions.

B. Inner region

As noted earlier, the details of the solution close to the contact lines cannot be resolved by the outer solution and we need to look into the dynamics of the inner regions, where the effect of slip is appreciable. The width of these inner regions is $O(\lambda)$. Hence, to examine the dynamics near the right contact point $x = a(t)$, we introduce the inner variables:

$$\Phi = \frac{h}{\lambda} \quad \text{and} \quad \xi = \frac{a-x}{\lambda}\,g_a,$$

where we set $g_a = g(a)$. By expressing Eq. (4) in terms of Φ and ξ we obtain

$$\dot{a}\frac{\partial \Phi}{\partial \xi} + g_a^3\frac{\partial}{\partial \xi}\left[\Phi^2(\Phi+1)\frac{\partial^3\Phi}{\partial \xi^3}\right] = 0 \tag{16}$$

to $O(\lambda^0)$, where, again, the variations of $g(x)$ are assumed to occur at length scales that are much longer than λ. By expressing the boundary conditions to solve Eq. (16) in terms of the inner variables, we obtain

$$\Phi|_{\xi=0} = 0 \quad \text{and} \quad \left.\frac{\partial \Phi}{\partial \xi}\right|_{\xi=0} = 1,$$

which are supplemented with the requirement that as we move toward the droplet bulk the linear terms dominate; i.e.,

$$\Phi/\xi^2 \to 0 \text{ as } \xi \to \infty.$$

Just as when treating the outer region, we also assume that the dynamics of the inner regions is quasistatic, which allows us to expand Φ in Eq. (16) as

$$\Phi = \Phi_0 + \dot{a}\Phi_1 + \cdots.$$

By taking the leading-order solution to be a wedge, i.e., $\Phi_0 = \xi$, the equation for Φ_1 becomes

$$\frac{\partial^3\Phi_1}{\partial \xi^3} = -\frac{1}{g_a^3\xi(\xi+1)},$$

to be solved subject to $\Phi_1|_{\xi=0} = \partial\Phi_1/\partial\xi|_{\xi=0} = 0$ and $\Phi_1/\xi^2 \to 0$ as $\xi \to \infty$. With these conditions, the leading-order slope of Φ_1 as we move away from the contact line is given by

$$\frac{\partial \Phi_1}{\partial \xi} \sim \frac{1+\ln\xi}{g_a^3}, \quad \text{as} \quad \xi \to \infty.$$

Hence, the asymptotic behavior of $\partial\Phi/\partial\xi$ as $\xi \to \infty$ becomes

$$\frac{\partial \Phi}{\partial \xi} \sim 1 + \frac{\dot{a}}{g_a^3}(1+\ln\xi), \quad \text{as} \quad \xi \to \infty,$$

or, in terms of the outer variables,

$$-\frac{\partial h}{\partial x} \sim g_a + \frac{\dot{a}}{g_a^2}\ln\left(eg_a\frac{a-x}{\lambda}\right), \quad \text{as} \quad \frac{a-x}{\lambda} \to \infty. \tag{17}$$

Likewise, to obtain $\partial h/\partial x$ as we move away from the contact point at $x = b(t)$, we follow similar arguments to finally obtain

$$\frac{\partial h}{\partial x} \sim g_b - \frac{\dot{b}}{g_b^2}\ln\left(eg_b\frac{x-b}{\lambda}\right), \quad \text{as} \quad \frac{x-b}{\lambda} \to \infty, \tag{18}$$

where $g_b = g(b)$.

C. Matching

The goal of our analysis is to match Eqs. (14) and (17) in some overlap region, where both asymptotic expansions are valid. However, we readily see that the coefficients in front of the x-dependent logarithmic terms do not match. Hence, an intermediate region that lies between the inner and outer regions is required to properly match the two solutions. The procedure for the intermediate regions may be carried out as in related studies (see, e.g., [11,49]), which eventually justifies rigorously why the matching can be carried out for $(\partial h/\partial x)^3$ instead of $\partial h/\partial x$. The details of this calculation are omitted here, and we directly consider the cubes of Eqs. (14) and (17), which upon matching yield

$$\frac{\phi^3 - g_a^3}{3} = \dot{a} \ln\left(g_a \frac{a-b}{e\lambda}\right) + \dot{b}. \tag{19}$$

By similar arguments, we match Eqs. (15) and (18) to obtain

$$\frac{\phi^3 - g_b^3}{3} = -\dot{b} \ln\left(g_b \frac{a-b}{e\lambda}\right) - \dot{a}. \tag{20}$$

Equations (19) and (20) constitute a system of linear equations for $\dot{a}$ and $\dot{b}$, from which we obtain

$$\dot{a} = \frac{\delta_a \ln\left(g_b \frac{a-b}{e\lambda}\right) + \delta_b}{\ln\left(g_a \frac{a-b}{e\lambda}\right) \ln\left(g_b \frac{a-b}{e\lambda}\right) - 1}, \tag{21a}$$

$$\dot{b} = -\frac{\delta_b \ln\left(g_a \frac{a-b}{e\lambda}\right) + \delta_a}{\ln\left(g_a \frac{a-b}{e\lambda}\right) \ln\left(g_b \frac{a-b}{e\lambda}\right) - 1}, \tag{21b}$$

where

$$\delta_a = \frac{\phi^3 - g_a^3}{3}, \quad \delta_b = \frac{\phi^3 - g_b^3}{3}, \tag{22}$$

and ϕ is given by Eq. (10). We readily see from Eqs. (21) that the droplet reaches equilibrium when both δ_a and δ_b vanish, i.e., when the local contact angles become equal to the apparent contact angle. Noteworthy is that in the absence of contact angle hysteresis due to other effects, equilibrium can only be attained if both angles at the contact points are equal to each other.

As a result of the asymptotic analysis we employed, we were able to reduce a nonlinear, fourth-order PDE into a much simpler system of ODEs, Eqs. (21), which gives the leading-order speeds of the two moving droplet fronts. In the following sections, we will examine various aspects of the solutions obtained by the system of ODEs, where we also make comparisons to the full PDE. We observe from Eqs. (21) that the droplet attains equilibria when the apparent contact angle, ϕ, equals the microscopic contact angle, $g(x)$, at the contact points.

It is important to emphasize that a crucial element of the above procedure is the smallness of λ. If λ is not small, the asymptotic analysis is expected to fail in describing the droplet dynamics. This is better illustrated if one considers symmetric spreading, i.e., spreading when $g(x)$ is an even function of x and initially we have that $a(0) = -b(0)$. In this case, $b(t) = -a(t)$, and $a(t)$ is found by solving the ODE

$$\frac{\phi^3 - g_a^3}{3} = \dot{a} \ln\left(g_a \frac{2a}{e^2\lambda}\right). \tag{23}$$

If $\phi > g(a)$, physically we expect to have advancing droplet fronts; i.e., $\dot{a} > 0$. For this to occur, the logarithmic term must be always positive and this happens for sufficiently small λ. If λ is not small, Eq. (23) may predict a receding droplet front, which is clearly nonphysical. Consequently, the full PDE needs to be considered instead, provided that the inertial effects do not become important, i.e., for λ up to $O(1)$ (see [57]).

IV. RESULTS

A. Dynamics

1. Comparison with full solution

Before presenting a detailed investigation of the dynamics of the system in Eqs. (21), we first compare its solution with that of the full PDE, Eq. (4), obtained numerically. The numerical solution of the full PDE is based on spectral differentiation in space and adaptive, semi-implicit time stepping, following similar ideas from the scheme outlined in the Appendix of Ref. [11].

For all cases presented here, the slip length is fixed at $\lambda = 10^{-5}$, unless otherwise stated. Initially, the droplet fronts are at $a(0) = -b(0) = 1$. In Fig. 2(a), we show the evolution

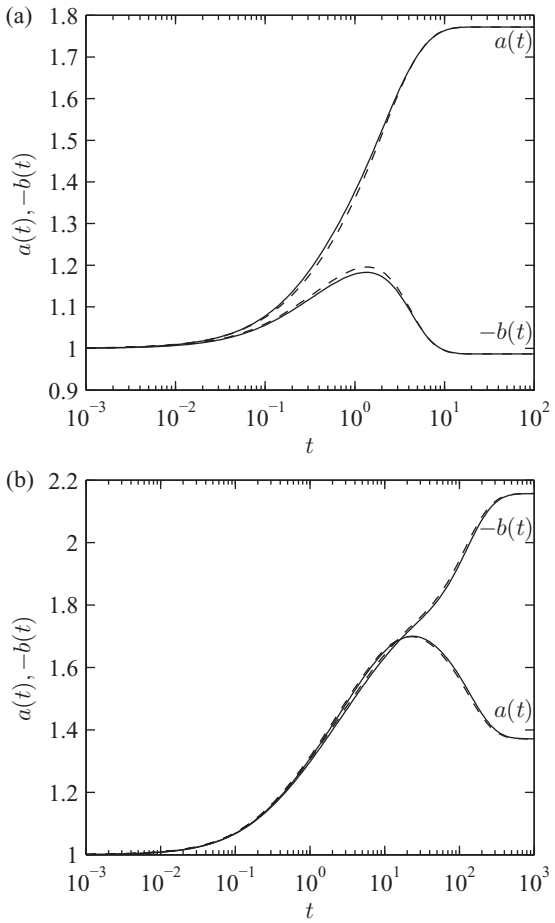

FIG. 2. Evolution of droplet fronts when $\lambda = 10^{-5}$ and $a(0) = -b(0) = 1$ for (a) $g(x) = 1 + 0.8 \sin 4x$ and (b) $g(x) = 1 + 0.05 \sin 4x$. Solid curves correspond to the solution of the coupled system of ODEs, Eqs. (21); dashed curves correspond to the solution of the PDE, Eq. (4).

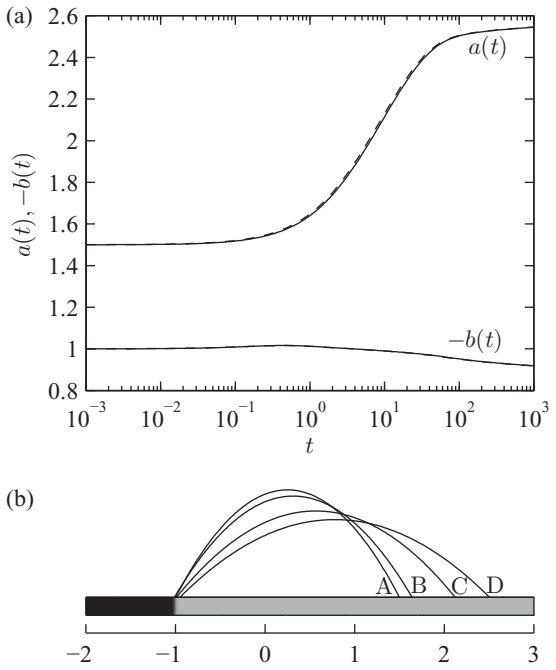

FIG. 3. (a) Evolution of droplet fronts on the substrate $g(x) = 1.5 - 0.5\tanh 50(x+1)$, $\lambda = 10^{-5}$. Solid curves correspond to the solution of the coupled equations (21a) and (21b) obtained from matching, dashed curves correspond to the solution of the full PDE, Eq. (4). (b) Evolution of the droplet free surface; curves A–D correspond to times $t = 0, 1, 10, 1000$, respectively.

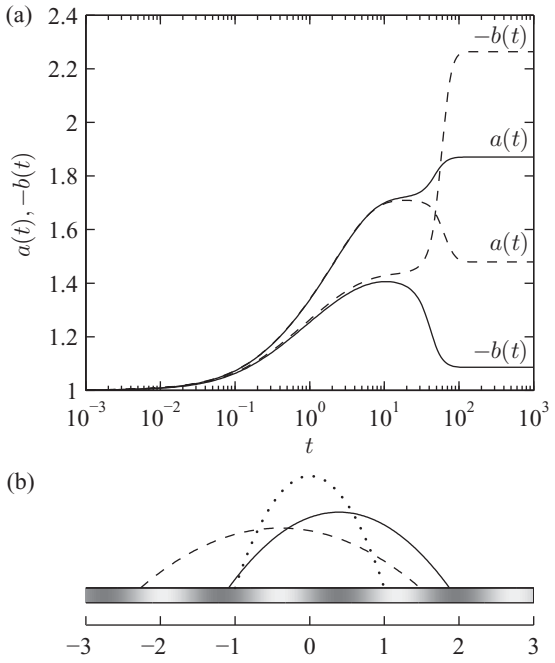

FIG. 4. Evolution of droplet fronts on the substrate $g(x) = 1 + 0.4\sin 4x$, $\lambda = 10^{-5}$ with $a(0) = -b(0) = 1$. (a) Solid curves correspond to the solution of the ODEs obtained by matching, Eqs. (21); dashed curves are the solution of the PDE, Eq. (4). A comparison of the two solutions shows that the left front, $b(t)$, always advances for the PDE, whereas for the ODEs it exhibits recession at later times. At equilibrium, both droplet fronts obtained from the PDE are shifted leftward compared to those obtained from the ODEs [higher $-b(t)$ and lower $a(t)$]. (b) The corresponding equilibrium droplet profiles. The dotted curve shows the initial droplet position. The substrate is shaded according to the color bar of Fig. 1

of the droplet fronts when $g(x) = 1 + 0.8\sin 4x$, where we observe an excellent agreement between the solutions to the PDE and the system of ODEs. Initially, both fronts advance, but at later times the left contact point recedes before eventually reaching equilibrium. The minor difference between the two solutions at the onset may be attributed to the relatively higher initial front speeds, which lie beyond the regime of validity of the matched asymptotics. However, it is evident that Eqs. (21) are able to satisfactorily capture the leading-order dynamics of Eq. (4). For a weaker heterogeneity profile, e.g., for $g(x) = 1 + 0.05\sin 4x$, there is an improved agreement between the two solutions shown in Fig. 2(b), as they are nearly indistinguishable. Now we observe a different behavior: The left droplet front advances toward equilibrium, whereas front recession is observed for the right contact point.

In general, a droplet avoids the less hydrophilic regions and moves toward more hydrophilic ones, in agreement with the results of previous studies (e.g., [45,50]). This effect is demonstrated with the heterogeneity profile $g(x) = 1.5 - 0.5\tanh 50(x+1)$, $a(0) = 1.5$, and $b(0) = -1$. Figure 3(a) shows the evolution curve for the droplet front locations based on Eqs. (21), which also exhibit excellent agreement with the solution to the PDE, Eq. (4). Figure 3(b) depicts the corresponding droplet shapes at different times. It is readily observed that the left droplet front is nearly pinned where the substrate wettability changes abruptly, whereas the right droplet front advances for all times. It should be noted here that the droplet never reaches equilibrium. The reason is because in this artificial substrate profile, there is no finite equilibrium, and the droplet is driven toward $+\infty$. However, the rate at which this occurs is exponentially small. Hence, in a more realistic setting, the droplet may be easily stopped by a tiny substrate defect, either chemical or topographical.

Despite the overall excellent agreement exhibited in Figs. 2 and 3 for the solutions to Eqs. (21) and Eq. (4), it should be emphasized that there may also exist cases for which their solutions are markedly different. To understand why this occurs, one needs to investigate the phase-plane dynamics of Eqs. (21) in detail, as done in a recent study for topographical substrates [56], where it was found that solutions to the governing PDE may deviate significantly from the solutions to the equations obtained by matched asymptotics, when the droplet fronts are initially located close to the boundaries of the basins of attraction of different fixed points. This is due to the fact that even a small perturbation, that is inherent in an asymptotic analysis due to our neglecting of the higher-order terms, may drive the dynamics to an entirely different equilibrium. To illustrate this effect, we consider in Fig. 4 the case when $g(x) = 1 + 0.4\sin 4x$. We readily see that the droplet fronts obtained by solving the equations resulting from the matching and those obtained by the PDE evolve in a different manner, eventually driving the droplet to different equilibria. We shall resume our discussion of the phase plane

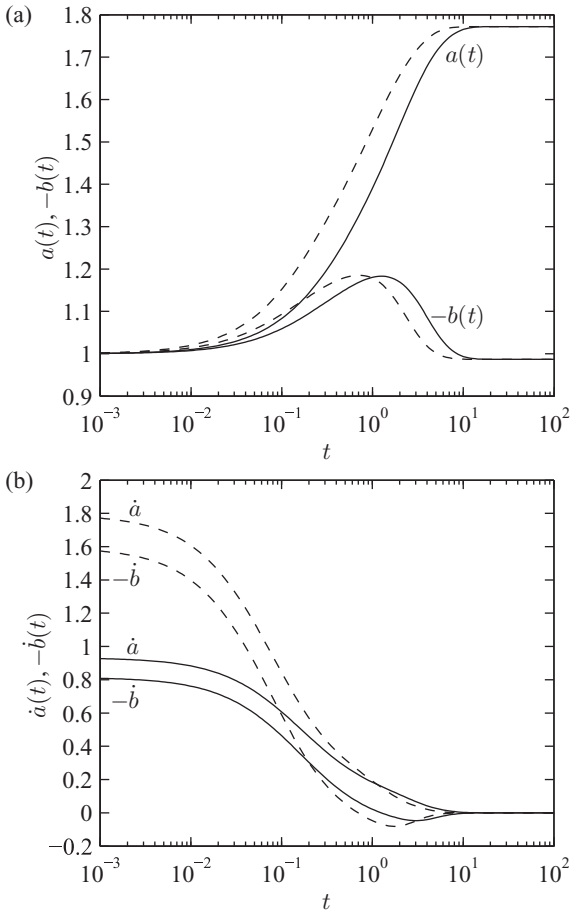

FIG. 5. Effect of λ: spreading on a substrate with $g(x) = 1 + 0.8 \sin 4x$ when $\lambda_1 = 2 \times 10^{-5}$ (solid curves) and $\lambda_2 = 2 \times 10^{-3}$ (dashed curves). (a) The evolution of the droplet fronts when $a(0) = -b(0) = 1$. (b) The corresponding velocities of the fronts.

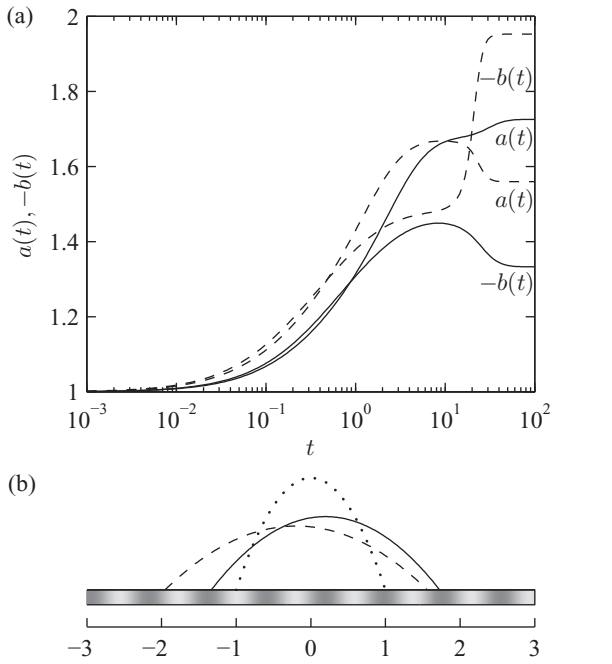

FIG. 6. Effect of λ: spreading on a substrate with $g(x) = 1 + 0.3 \sin 8x$, when $\lambda_1 = 2 \times 10^{-5}$ (solid curves) and $\lambda_2 = 2 \times 10^{-3}$ (dashed curves). (a) The evolution of the droplet fronts when $a(0) = -b(0) = 1$. (b) The corresponding equilibrium droplet profiles; the dotted curve refers to the initial droplet shape. The substrate is shaded according to the color bar of Fig. 1.

when investigating the nature of the droplet equilibria in the following sections.

2. *Effect of slip*

Having established with numerical experiments the validity of the ODEs obtained by matching, we will now consider the effect of slip on the dynamics. Slip originates from processes occurring at molecular length scales, and in our model we have assumed that it is constant everywhere as discussed in Sec. II. Even though a space-dependent λ might have been somewhat more realistic, we chose to keep it constant. This simplifies our analysis; after all our principal aim is to study the qualitative characteristics of the dynamics. Besides, slip does not affect the equilibria and their stability. Moreover, Eqs. (21) indicate that the speed of the droplet fronts is only logarithmically dependent on λ and as a consequence the influence of λ on the approach to equilibrium is generally weak.

To show how precisely the dynamics depend on λ, we performed simulations using Eqs. (21) for a substrate with $g(x) = 1 + 0.8 \sin 4x$ and two slip lengths differing by a factor of 100, namely $\lambda_1 = 2 \times 10^{-5}$ and $\lambda_2 = 2 \times 10^{-3}$. In Fig. 5(a) we show the evolution of the moving fronts when $a(0) = -b(0) = 1$ and observe that the overall qualitative behavior is not affected by the different slip, despite the significantly faster front speeds for the longer slip length, λ_2 [see Fig. 5(b)]. This qualitative agreement is generally expected, even if the disparity between the slip lengths is large. However, there can also exist cases for which different slip lengths yield significantly different dynamics, for initial conditions located near the saddle point manifolds, as previously mentioned when comparing with solutions to the full PDE. To illustrate such effects, we show in Fig. 6(a) the evolution of $a(t)$ and $b(t)$ resulting from Eqs. (21) for a substrate with $g(x) = 1 + 0.3 \sin 8x$ and the same parameters as in Fig. 5. We now observe that the change in λ is sufficient to lead the droplet to a different equilibrium in the long-time limit [see Fig. 6(b)].

3. *Stick-slip and hysteresis-like effects*

For the substrate $g(x) = 1 + 0.3 \sin 100x$, $a(0) = -b(0) = 1$, in which the variations in microscopic contact angle occur at shorter length scales, we observe from Fig. 7(a) that the speed of the droplet fronts exhibit fluctuations in time, before eventually vanishing in the long-time limit. This behavior is manifested as a brief sticking and slipping of the droplet fronts, which may also be visualized in the evolution plot of the ratio of the apparent to microscopic contact angles [see Fig. 7(b)]. Typically, the sticking and slipping of the droplet fronts becomes more common when both the wavelength of the heterogeneities and their amplitude are small, i.e., when the number of equilibria accessible to the droplet increase.

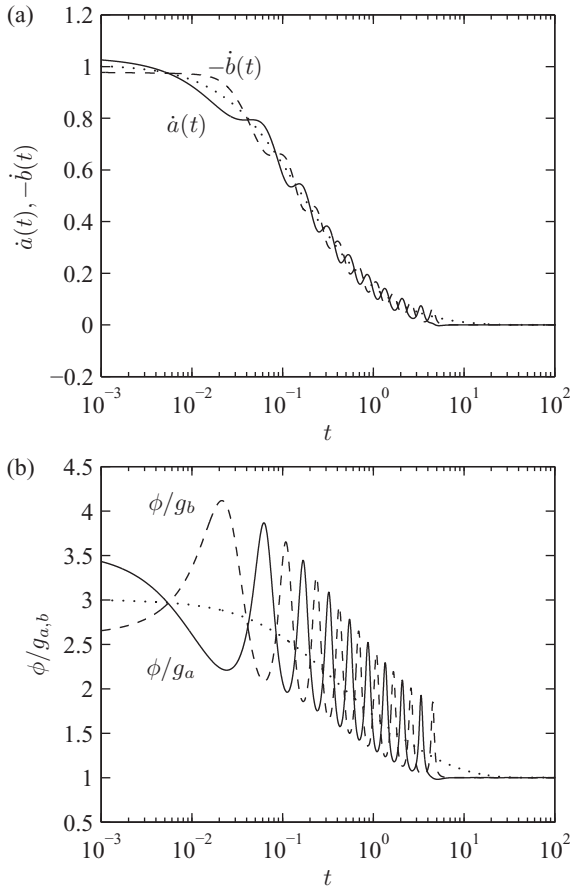

FIG. 7. Spreading on a substrate $g(x) = 1 + 0.3 \sin 100x$ (solid and dashed curves for the right and left fronts, respectively) compared to spreading over the ideal substrate, $g(x) = 1$ (dotted curves). (a) Time evolution of velocity of contact lines showing stick-slip type behavior. (b) Evolution of the ratio of contact angles $\phi/g_{a,b}$.

Even though hysteresis in the contact angle was not assumed in our model (i.e., the existence of both an advancing and a receding critical angle), it is still possible to observe a hysteresis-like effect induced by the chemical heterogeneities. This is due to the presence of multiple equilibria that are able to pin the droplet to different stable states. This effect is better demonstrated with a plot of the apparent contact angle as a function of the contact line speed, as shown in Fig. 8. Two curves are shown there: The first corresponds to initially advancing droplet fronts $[a(0) = -b(0) = 1]$ and the second to initially receding droplet fronts $[a(0) = -b(0) = 3]$. It is worth emphasizing the disparity in the speeds of the receding and advancing fronts, which appears to be a common feature for both chemical heterogeneities and topographical substrates [11]. In the end, we observe that two distinct equilibrium angles are attained, differing by $\Delta\phi \approx 0.51$. As with the stick-slip behavior, this hysteresis-like effect is more likely as the possible stable states become more dense. We shall return to this and related effects in our discussion on the phase-plane dynamics that follows.

B. Phase-plane analysis

Capturing the spreading dynamics of the full nonlinear PDE with a set of two coupled ODEs also allows us to investigate

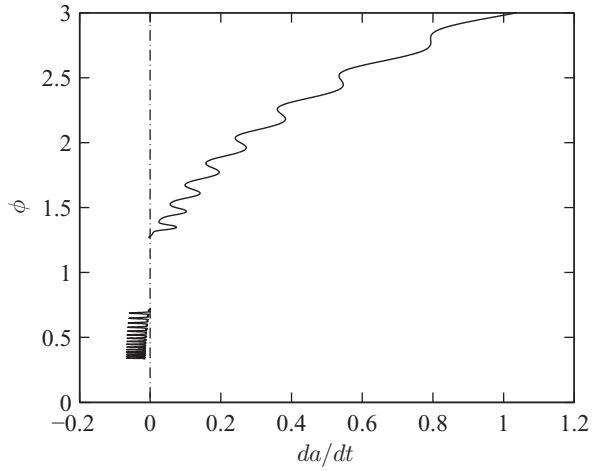

FIG. 8. Plot of apparent contact angle as a function of the velocity of a moving droplet front for the substrate $g(x) = 1 + 0.3 \sin 100x$.

the dynamics on the phase plane. By doing so, we aim to extract generic dynamic features, which would otherwise have been difficult to identify, by, e.g., integrating at random the governing equations for different initial conditions. Figure 9(a) depicts the a-b phase plane of Eqs. (21) together with its direction field, for the substrate $g(x) = 1 + 0.8 \sin 4x$. We observe three types of equilibria, namely stable and unstable nodes and saddle points. Due to the assumed periodicity in the chemical heterogeneities, the equilibria also exhibit a periodic structure. Taking into account this structure, we can identify in Fig. 9(a) two equilibria for which there is wetting enhancement (points q_1 and q_2), and one for which there is wetting inhibition (point q_3). It is important to emphasize that assessments on wetting are made with respect to the homogeneous substrate, for which we defined the reference angle and $g(x) = 1$. Consequently, when we have $\phi > 1$ ($\phi < 1$) at equilibrium, we refer to these equilibria as wetting inhibiting (enhancing).

Naturally, these equilibria must correspond to the stationary points of the total interfacial energy of the system, which in dimensional form is given by

$$\mathcal{E} = \int_b^a \left[\sigma\sqrt{1 + \left(\frac{\partial H(x)}{\partial x}\right)^2} + \sigma_{ls}(x) - \sigma_{sg}(x)\right] dx,$$

where $\sigma_{ls}(x)$ and $\sigma_{sg}(x)$ are the spatially varying surface tensions of liquid-solid and solid-gas interfaces, respectively. By making use of the expression for the local contact angle predicted by Young's equation, $\sigma \cos\alpha(x) = \sigma_{sg}(x) - \sigma_{ls}(x)$, the long-wave form of $\mathcal{E}$, E, becomes

$$E = \int_b^a \left[\left(\frac{\partial h_0(x)}{\partial x}\right)^2 + g^2(x)\right] dx,$$

in nondimensional units, where $h_0(x)$ is the leading-order outer solution, Eq. (9).

For a given $g(x)$, E is a function of the position of droplet fronts, a and b. As an example, we show in Fig. 9(b) a plot of the interfacial energy, $E(a,b)$, corresponding to $g(x) = 1 + 0.8 \sin 4x$, together with some representative contours projected on the $E = 0$ plane. The plot, as well as our calculation, shows that, indeed, the stationary points of E correspond to

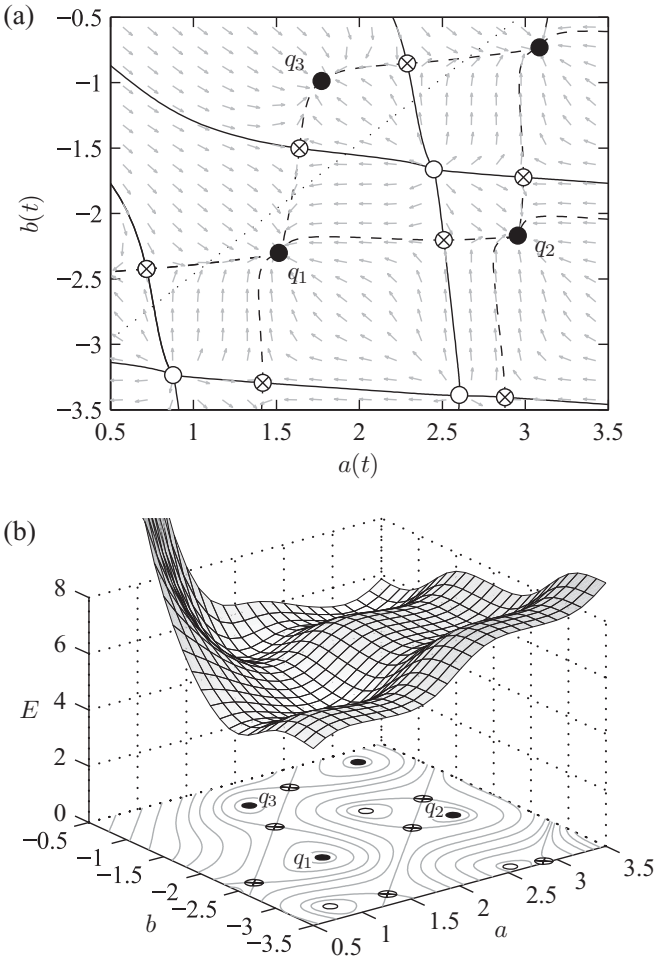

FIG. 9. (a) The a-b phase plane for $g(x) = 1 + 0.8 \sin 4x$. Solid and open circles represent the stable and unstable nodes, respectively, and the crossed circles represent the saddle points. Solid and dashed lines refer to the stable and unstable manifolds for the saddle nodes, respectively, whereas the dotted line shows the line of equilibria when $g(x) = 1$. (b) Plot of interfacial energy as a function of position of the droplet fronts for $g(x) = 1 + 0.8 \sin 4x$, along with some representative contours projected on the $E = 0$ plane (gray curves). The stationary points of E correspond to the fixed points of the phase plane in (a).

the fixed points of Eqs. (21) shown on the a-b phase plane of Fig. 9(a). It is clear, however, that energy considerations alone cannot predict the dynamic droplet behavior, which is highly dependent on the initial conditions. On the contrary, a phase plane analysis facilitates such assessments and the extraction of generic dynamic features.

In order to investigate whether other types of equilibria can exist apart from the ones observed in Fig. 9(a) (e.g., spiral fixed points or centers), we need to consider a linearization of the system (21) about its equilibria. From Eqs. (21) we find

$$a_\infty = b_\infty + 2\sqrt{3}/\sqrt{\phi_\infty}, \tag{24}$$

where a_∞ and b_∞ correspond to the equilibrium positions of the contact lines and ϕ_∞ is the equilibrium contact angle, which satisfies $\phi_\infty = g(a_\infty) = g(b_\infty)$. For chemically homogeneous substrates, Eq. (24) predicts a continuum of stable equilibria, shown as dotted lines in the phase-plane plots [see, e.g., Fig. 9(a)]. Naturally, these equilibria are translationally invariant, but this invariance is broken with the introduction of a chemical structure, for which we can have at most countably infinite equilibria.

Next, consider the linearized system (21) about a fixed point to obtain

$$\begin{pmatrix} \dot{a} \\ \dot{b} \end{pmatrix} = \mathbf{J} \begin{pmatrix} a - a_\infty \\ b - b_\infty \end{pmatrix},$$

where $\mathbf{J}$ corresponds to the Jacobian matrix evaluated at the fixed point (a_∞, b_∞). In order to have either spiral fixed points or centers, the Jacobian matrix must have complex eigenvalues. For this to happen, the discriminant of the characteristic polynomial of $\mathbf{J}$, D, must be negative. After some algebra, D evaluated at (a_∞, b_∞) is written as

$$D = \frac{\phi_\infty^4}{3A^2(A-2)^2}\left\{3A(A-2)[g'(a_\infty) + g'(b_\infty)]^2 + \left[2\phi_\infty^{3/2}A + \sqrt{3}[g'(a_\infty) - g'(b_\infty)]\right]^2\right\},$$

where $A = \ln(2\sqrt{3\phi_\infty}/\lambda)$. Since the second term in the curly brackets is always positive, it is clear that the only way for D to become negative is that $0 < A < 2$. This, however, can only occur for unrealistically large λ, in a regime where our matched asymptotics are expected to fail, as we have already pointed out in Sec. III C. Consequently, at least for realistically small λ, no matter how $g(x)$ is chosen, it is impossible to excite any type of oscillatory behavior. Exploratory numerical experiments with the full PDE Eq. (4) suggest that this behavior persists for larger λ as well.

1. Localized defects

Chemical heterogeneities may be utilized as a means to control droplet behavior, by, e.g., trapping the droplet between two localized defects. For the sake of illustration, consider a chemical profile of the form

$$g(x) = 1 + \epsilon[\text{sech } 20(x + s/2) + \text{sech } 20(x - s/2)],$$

which consists of two sufficiently isolated "bumps" separated by a distance s. Here we take $s \geqslant 1$ so that the effects of one bump do not affect the other and $g(\pm s/2) \approx 1 + \epsilon$. We are interested in determining under what conditions the localized defects are able to trap a droplet that is initially located somewhere between them. In a more general setting, one could have allowed for different amplitudes in the two bumps, but this simpler problem allows us to capture the essential qualitative features as we change the "strength" of the isolated chemical defects, ϵ. The case of a single defect appears to be less interesting, as the velocities toward equilibrium are exponentially small; for a profile with a chemical "bump" the droplet moves toward infinity, whereas for a chemical "dimple" the droplet has a single stable equilibrium centered about the defect. The effects of a single defect on a far away droplet are extremely small and the droplet motion is virtually unaffected by it.

For our analysis we fix $s = 3$. Instead of considering the typical a-b phase plane, we consider the ℓ-d phase plane,

where ℓ is defined as the location of the droplet midpoint along the x axis and d is the droplet "radius":

$$\ell = (a+b)/2 \quad \text{and} \quad d = (a-b)/2.$$

This transformation is introduced to facilitate the visualization of the different regimes we observe as ϵ varies. For sufficiently small ϵ, there are no stable fixed points, and the droplet eventually escapes from the defects. For initial conditions that are initially located symmetrically about the origin, i.e., when $\ell(0) = 0$, the droplet eventually attains an equilibrium radius that roughly corresponds to the equilibrium radius on the reference substrate; i.e., $d(\infty) \approx \sqrt{3} > 3/2$. In Fig. 10(a) we show a snapshot of the phase plane when $\epsilon = 0.2$, which illustrates this behavior.

The absence of stable equilibria persists until we reach a critical ϵ, ϵ_c, beyond which a stable node appears, which lies symmetrically about $\ell = 0$. When $s = 3$, we readily observe that $\epsilon_c \approx 1/3$. In Fig. 10(b), we show a snapshot of the phase plane for $\epsilon = 0.4 > \epsilon_c$, where we clearly see the newly emerged equilibria. To get a measure of the admissible initial conditions that may be used to trap the droplet between the chemical defects, we record the locations of the basin boundaries when $d(0) = 1$, which also allows us to determine the width of the basin of attraction, $\Delta\ell$ [see Fig. 10(b)]. As ϵ is increased further, the basin of attraction of the fixed point enlarges, which in turn implies that given $d(0) = 1$, the range of $\ell(0)$ that eventually traps the droplet becomes larger, too. This is conveniently depicted on the regime diagram of Fig. 10(c), where we plot $\ell(0)$ as a function of ϵ, with the shaded region corresponding to initial conditions for trapped droplets. This regime diagram is to be taken as an estimate of the actual diagram for the full PDE, since as we have noted earlier, in the vicinity of the boundaries of the basins of attraction our theory may potentially fail. It should also be noted that the actual "basin of attraction" of the full PDE is infinite-dimensional, but nevertheless the information we can infer from Fig. 10(c) is sufficient to describe the trapping of a droplet between two defects, at least in qualitative terms.

At the critical ϵ, one eigenvalue of the Jacobian of the linearized system vanishes. At this fixed point, the droplet fronts are located at the maxima of $g(x)$, $x \approx \pm s/2$. Using Eq. (24), we find the radius at equilibrium, $d_\infty = \sqrt{3/(1+\epsilon_c)}$, from which we approximately deduce that

$$\epsilon_c \approx \frac{12}{s^2} - 1 \tag{25}$$

with exponentially small corrections. As a consequence, for $s < 2\sqrt{3}$ and when $\epsilon > \epsilon_c > 0$ a stable node appears that can potentially trap a droplet with advancing fronts, whereas for $s > 2\sqrt{3}$ and when $\epsilon < \epsilon_c < 0$, the stable node can potentially trap a droplet with receding fronts. This result is consistent with the observation by Thiele and Knobloch, where the less hydrophilic regions can trap advancing fronts and the more hydrophilic ones can trap receding fronts [45].

2. *Patterned substrates*

Chemically patterned substrates are specially treated substrates that are composed of periodically alternating regions of different wettability. As in the preceding section, we employ

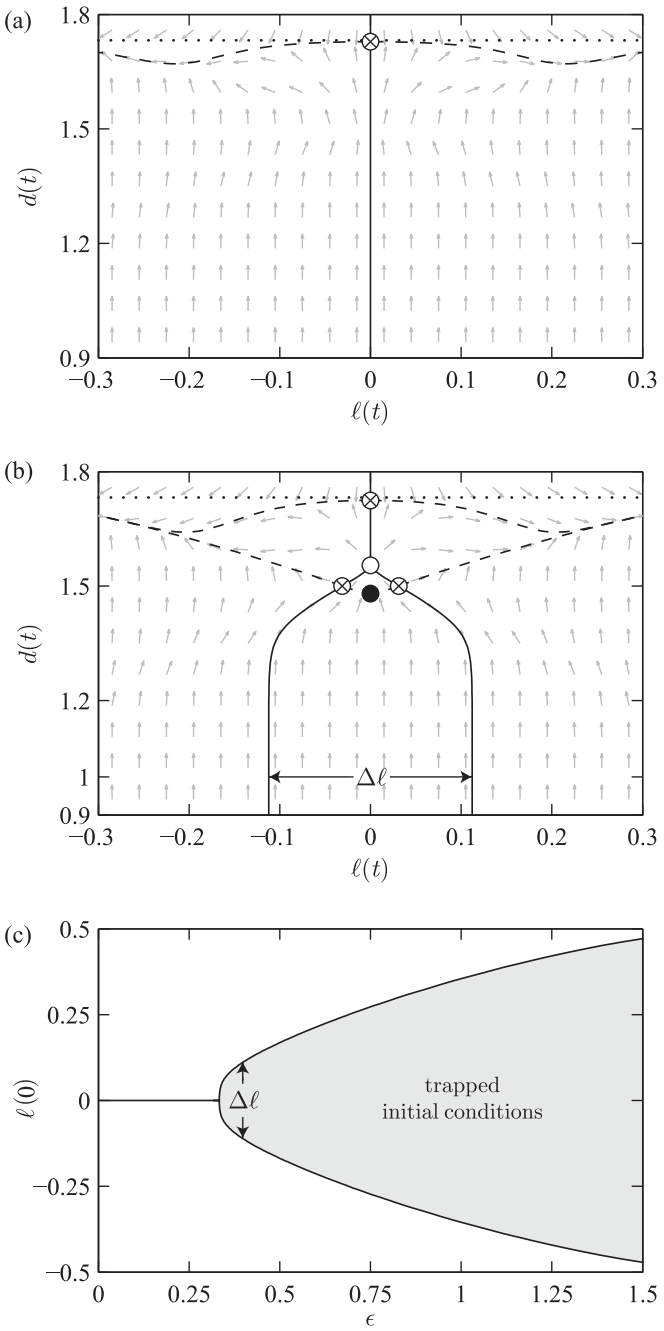

FIG. 10. (a),(b): The ℓ-d phase plane for the localized substrate $g(x) = 1.0 + \epsilon[\text{sech } 20(x + 1.5) + \text{sech } 20(x - 1.5)]$ for (a) $\epsilon = 0.2$ and (b) $\epsilon = 0.4$. For the different lines and symbols refer to Fig. 9. (c) Regime diagram showing the initial droplet locations for which we have trapped droplet fronts as a function of ϵ.

a phase-plane analysis to extract qualitative features of the hysteresis-like effect induced by the varying substrate chemistry. We chose to model such substrates using a heterogeneity function of the form

$$g(x) = 1 + \varepsilon \tanh(m \cos kx), \tag{26}$$

which consists of a periodic array of plateau regions that have different wettability characteristics (see Fig. 11). Here ε is a measure of the wettability contrast between the two regions and k is the wave number of the profile. The parameter m controls

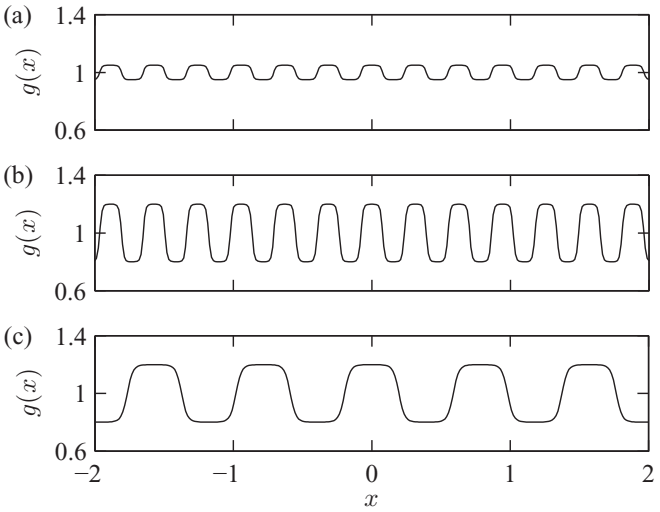

FIG. 11. Plots of the heterogeneity function $g(x) = 1.0 + \varepsilon \tanh(3 \cos kx)$. (a) $\varepsilon = 0.05, k = 20$; (b) $\varepsilon = 0.2, k = 20$; and (c) $\varepsilon = 0.2, k = 8$.

how abruptly the transition between the two regions occurs; as m increases, $g(x)$ approaches a square wave form and as it decreases, it approaches a pure harmonic. We have fixed $m = 3$ so that we have relatively sharper transitions than having a pure harmonic and, at the same time, the phase-plane snapshots are sufficiently smooth for the clarity of presentation. Since our principal aim is to assess the chemically induced hysteresis, we consider the phase plane for a different set of variables, the apparent contact angle, ϕ, and the displacement of the droplet midpoint, ℓ.

We first take a substrate with $\varepsilon = 0.05$ and $k = 20$, a snapshot of which is shown in Fig. 11(a). Accounting for the substrate periodicity, we only observe three distinct equilibria: one saddle point and two stable nodes lying above and below $\phi = 1$, the reference contact angle [see Fig. 12(a)]. More importantly, we observe that these stable equilibria are readily accessible for both initially advancing and initially receding fronts. For example, when we have $\ell(0) = 0$ and $\phi(0) = 3$ at the onset, the equilibrium attained at the end is wetting enhancing, whereas the equilibrium corresponding to $\ell(0) = -0.2$ and $\phi(0) = 3$ is wetting inhibiting. Nevertheless, the difference between the two equilibrium angles is small because the wettability contrast is fairly low.

As the wettability contrast increases, e.g., for $\varepsilon = 0.2$ and $k = 20$ [see Fig. 11(b)], the phase plane becomes richer due to emergence of new stable and unstable states. In this particular example, we now have 8 distinct equilibria, only 3 of which correspond to stable states [see nodes p_1, p_2, and p_3 in Fig. 12(b)]. Since in a typical spreading experiment we initially have that $\phi(0) > 1 + \varepsilon$, we readily see that the only equilibrium that is accessible to advancing fronts is p_1. On the other hand, initially receding fronts, for which $\phi(0) < 1 - \varepsilon$, have access to the stable nodes p_2 and p_3 only. Given that the notion of wetting enhancement and inhibition is introduced with respect to advancing fronts, we may infer from the phase-plane plot of Fig. 12(b) that the substrate is wetting inhibiting with respect to the reference angle. However, it is important to emphasize that we now have two possible values

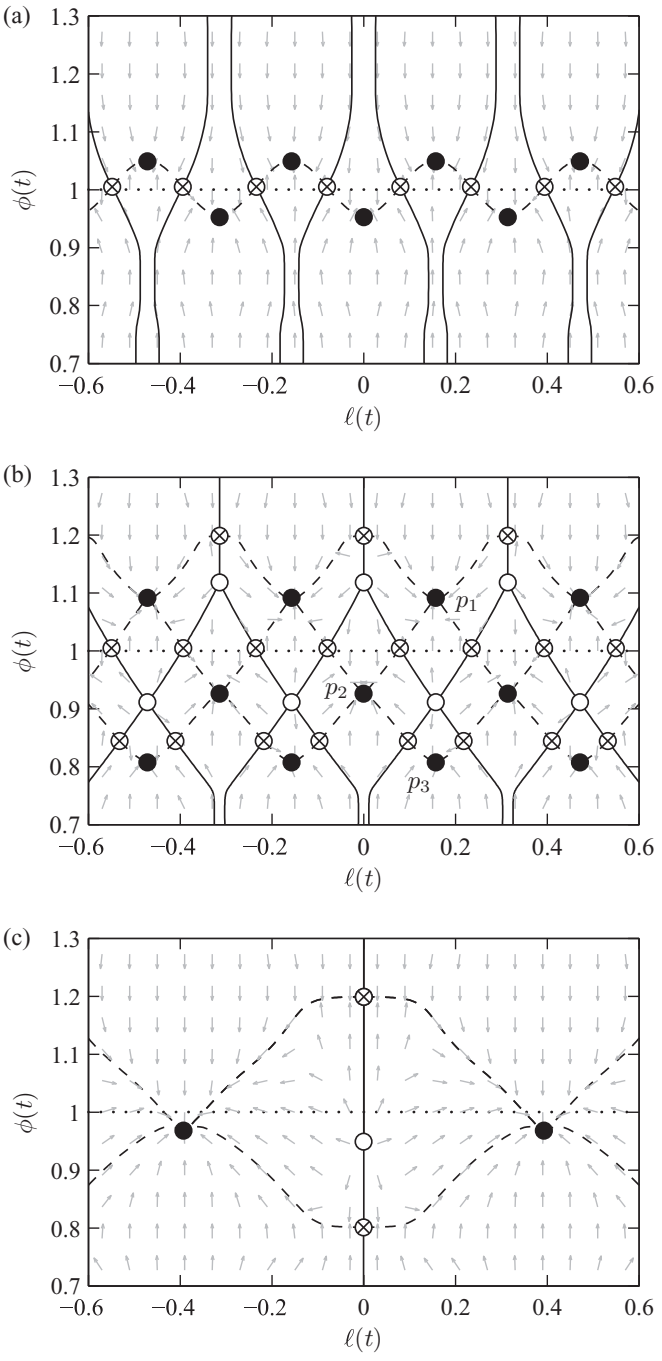

FIG. 12. The ℓ-ϕ phase plane for $g(x) = 1.0 + \varepsilon \tanh(3 \cos kx)$. (a) $\varepsilon = 0.05$, $k = 20$; (b) $\varepsilon = 0.2$, $k = 20$; and (c) $\varepsilon = 0.2$, $k = 8$. For the different lines and symbols refer to Fig. 9.

for contact angle hysteresis between advancing and receding fronts, with the difference in the contact angle between the fixed points p_1 and p_3 being more appreciable compared to that of points p_1 and p_2. As generally expected, a further increase in the wettability contrast would amplify the observed hysteresis effect. On the other hand, the wettability contrast is not the only factor that influences wetting, but also the wave length or wave number of the chemical heterogeneities. For example, if we keep the wettability contrast at $\varepsilon = 0.2$ and, at the same time, reduce the wave number to $k = 8$ [see

Fig. 11(c)], we now have a single stable configuration, which enhances wetting relative to the reference angle, $\phi = 1$ [see Fig. 12(c)].

To further investigate the effect of k, we consider the droplet equilibria for a wetting profile of the form prescribed by Eq. (26), which must satisfy $\cos(ka_\infty) = \cos(kb_\infty)$. From this relation, we can easily extract two different possibilities, namely $\ell_\infty = \pi n/k$ and $\phi_\infty = 3k^2/(n^2\pi^2)$, where n is an integer. Hence, the distinct droplet equilibria can either be located at $\ell_\infty = 0, \ell_\infty = \pi/k$ or the corresponding ℓ_∞ for which

$$\phi_\infty = 3k^2/(n^2\pi^2). \tag{27}$$

For Eq. (27), k must lie between $n\pi\sqrt{(1-\varepsilon)/3}$ and $n\pi\sqrt{(1+\varepsilon)/3}$ so that $1-\varepsilon < \phi_\infty < 1+\varepsilon$. To get a better picture for the variation of ϕ_∞ and its stability as k varies, numerical continuation techniques were used to trace the bifurcation curves of all droplet equilibria when $\ell_\infty = 0$ and $\ell_\infty = \pi/k$. The results of this calculation are depicted in Fig. 13, where ϕ_∞ is plotted as a function of k. They reveal intricate bifurcation events during which new equilibria appear or change stability characteristics due to coalescence with nearby equilibria. From such a plot one can identify all possible values of ϕ_∞, as for example in Fig. 13(b) where we clearly mark the stable equilibria corresponding to $k = 20$ [see also Fig. 12(b)].

From the above discussion, we may conclude that making quantitative statements as to how the contact angle is affected by heterogeneities in this geometry is a formidable task, apart from the observation that as the wave number increases, it is more likely for the equilibrium contact angle for a spreading droplet to be close to the maximum, $\phi_\infty = 1+\varepsilon$. To demonstrate the inability of Eq. (1) to describe the configurations we just outlined, we consider a substrate composed of two different materials with equilibrium contact angles, $1+\varepsilon$ and $1-\varepsilon$. These angles correspond roughly to the maximum and minimum microscopic contact angles for $g(x)$, Eq. (26). Assuming equal area fractions, Eq. (1) becomes

$$\phi_C = \sqrt{1+\varepsilon^2}, \tag{28}$$

which, in the limit $\varepsilon \ll 1$, predicts wetting inhibition with hysteresis of $O(\varepsilon^2)$ with respect to the reference angle. Clearly, Eq. (28) is independent of k, and as a result completely fails to capture any of the observations that were made above. Thus, it is not surprising that none of the test cases presented in Fig. 12 agree with the prediction of Eq. (28). Even when we take $\varepsilon = 0.2$ and $k = 20$ [Fig. 12(b)] for which there is indeed wetting inhibition, the observed effect is $O(\varepsilon)$, which is higher compared to the prediction of Eq. (28). Such significant deviations could be due to the anisotropy of the chemical features [28].

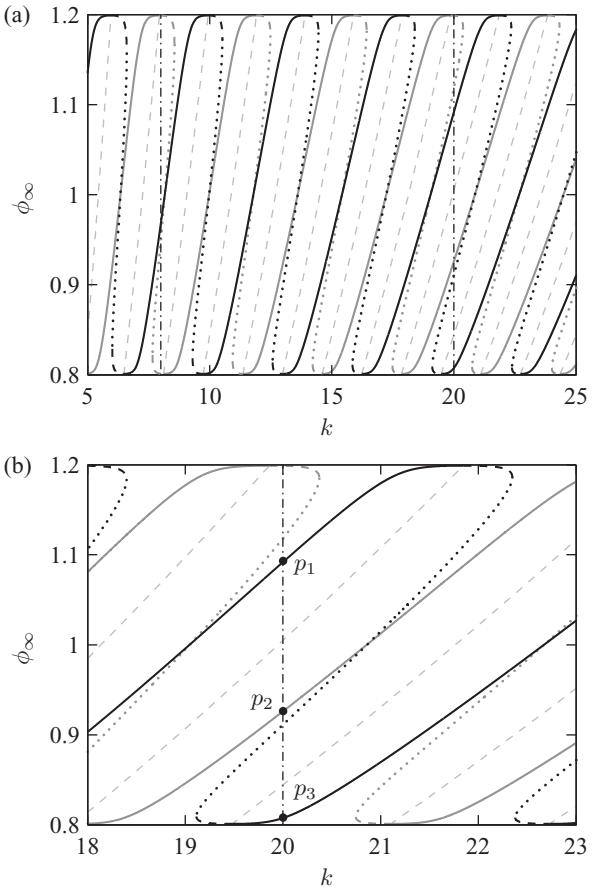

FIG. 13. (a) Evolution of equilibrium contact angles along with their stability, ϕ_∞, as k varies for $g(x) = 1 + 0.2\tanh(3\cos kx)$. Solid lines correspond to stable nodes, dashed lines to saddle points, and the dotted lines to unstable nodes. The dashed-dotted line demarcates the cases when $k = 8$ and $k = 20$, whose phase planes appear in Figs. 12(b) and 12(c), respectively. The gray dashed curves which are nearly diagonal and linear correspond to the curves of Eq. (27) for different n. The black and gray curves correspond to the bifurcation curves for the equilibria located at $\ell_\infty = \pi/k$ and $\ell_\infty = 0$, respectively. As k increases, these curves become sheared toward the right, thus allowing for more equilibria for any given k. (b) Detail of (a) near $k = 20$ marking the equilibria that correspond to those exhibited in Fig. 12(b).

V. CONCLUSION

We have considered the surface-tension-dominated motion of a two-dimensional, partially wetting droplet on a chemically heterogeneous substrate. We utilized a single evolution equation for the droplet thickness obtained from a long-wave expansion of the Stokes equations. The stress singularity at the contact line was alleviated with the Navier slip condition, wherein the slip length was taken to be constant along the heterogeneous substrate due to its generally weak influence on the dynamics. We thus introduced the chemical heterogeneities by assuming spatial variations in the microscopic contact angle, which naturally enter the problem as boundary conditions. In the limit of small capillary numbers, the droplet motion can be treated quasistatically, with the time dependence entering the problem through the contact line locations. These modeling assumptions allowed us to analyze the dynamics using singular perturbation theory, by considering separately the free surface in the vicinity of the contact lines and the fluid bulk. By asymptotically matching the solutions in the contact line regions and bulk, we obtained a set of coupled ODEs for the velocity of the moving fronts.

The solution to the set of ODEs obtained from matching was verified by direct comparisons with the governing PDE. In general, there is excellent agreement between the two. However, we found that it is possible for the two solutions to exhibit discordant evolution characteristics whenever the initial location of the two droplet fronts is sufficiently close to saddle point manifolds. These cases are commonly manifested as evolutions to different stable equilibria. The existence of multiple equilibria suggested that there can exist a hysteresis-like effect induced by the chemical heterogeneities, which was demonstrated by our simulations. This subsequently prompted our investigation of the phase plane of the two droplet fronts, which facilitated the extraction of more general spreading characteristics. In particular, we investigated the effect of localized defects and found that a droplet can be trapped between them, depending on the initial location of the droplet fronts and provided that the strength of the heterogeneities exceeds some threshold. Finally, we have considered the effects of substrates composed of periodic regions that have different wetting characteristics and we demonstrated that the Cassie relation cannot explain the observed behaviors.

The lack of experimental studies for the two-dimensional geometry we considered precludes any direct comparisons of our theory with experiments. We have demonstrated, however, that the two-dimensional problem is nontrivial and our study can be viewed as a first step in the consideration of additional effects and complexities, e.g., random chemically heterogeneous substrates (by appropriately extending the stochastic methodologies developed in Refs. [12–14] for random topographical substrates) and three-dimensional effects. Nevertheless, we believe that the present model is able to capture many of the qualitative effects of chemical heterogeneities for a three-dimensional geometry. We also hope that it can motivate careful experiments to investigate contact line motion in a direction normal to two-dimensional chemical heterogeneities as is the case here.

ACKNOWLEDGMENTS

We acknowledge financial support from EU-FP7 ITN Multiflow, EPSRC Platform Grant No. EP/E046029, EPSRC Grant No. EP/F009194, and ERC Advanced Grant No. 247031.

[1] E. B. Dussan V., Annu. Rev. Fluid Mech. **11**, 371 (1979).
[2] P.-G. de Gennes, Rev. Mod. Phys. **57**, 827 (1985).
[3] A. A. Darhuber and S. M. Troian, Annu. Rev. Fluid Mech. **37**, 425 (2005).
[4] D. Bonn, J. Eggers, J. Indekeu, J. Meunier, and E. Rolley, Rev. Mod. Phys. **81**, 739 (2009).
[5] L. H. Tanner, J. Phys. D: Appl. Phys. **12**, 1473 (1979).
[6] O. V. Voinov, Fluid Dyn. **11**, 714 (1976).
[7] P. Neogi and C. A. Miller, J. Colloid Interface Sci. **86**, 525 (1982).
[8] R. G. Cox, J. Fluid Mech. **168**, 169 (1986).
[9] G. McHale, M. I. Newton, S. M. Rowan, and M. Banerjee, J. Phys. D: Appl. Phys. **28**, 1925 (1995).
[10] P. Ehrhard and S. H. Davis, J. Fluid Mech. **229**, 365 (1991).
[11] N. Savva and S. Kalliadasis, Phys. Fluids **21**, 092102 (2009).
[12] N. Savva, S. Kalliadasis, and G. A. Pavliotis, Phys. Rev. Lett. **104**, 084501 (2010).
[13] N. Savva, G. A. Pavliotis, and S. Kalliadasis, J. Fluid Mech. **672**, 358 (2011).
[14] N. Savva, G. A. Pavliotis, and S. Kalliadasis, J. Fluid Mech. **672**, 384 (2011).
[15] K. H. Chu, R. Xiao, and E. N. Wang, Nature Mater. **9**, 413 (2010).
[16] N. A. Malvadkar, M. J. Hancock, K. Sekeroglu, W. J. Dressick, and M. C. Demirel, Nature Mater. **9**, 1023 (2010).
[17] D. Quéré, Rep. Prog. Phys. **68**, 2495 (2005).
[18] Z. Nie and E. Kumacheva, Nature Mater. **7**, 277 (2008).
[19] C. Sodtke, V. S. Ajaev, and P. Stephan, J. Fluid Mech. **610**, 343 (2008).
[20] C. Decamps and J. D. Coninck, Langmuir **16**, 10150 (2000).
[21] A. B. D. Cassie, Discuss. Faraday Soc. **3**, 11 (1948).
[22] L. Gao and T. J. McCarthy, Langmuir **23**, 3762 (2007).
[23] G. McHale, Langmuir **23**, 8200 (2007).
[24] M. Nosonovsky, Langmuir **23**, 9919 (2007).
[25] M. V. Panchagnula and S. Vedantam, Langmuir **23**, 13242 (2007).
[26] A. Marmur and E. Bittoun, Langmuir **25**, 1277 (2009).
[27] L. Gao and T. J. McCarthy, Langmuir **25**, 7249 (2009).
[28] P. S. Swain and R. Lipowsky, Langmuir **14**, 6772 (1998).
[29] R. Crawford, L. K. Koopal, and J. Ralston, Colloids Surf. **27**, 57 (1987).
[30] G. Yamauchi, J. D. Miller, H. Saito, K. Takai, T. Ueda, H. Takazawa, H. Yamamoto, and S. Nislhi, Colloids Surf. A **116**, 125 (1996).
[31] J. T. Woodward, H. Gwin, and D. K. Schwartz, Langmuir **16**, 2957 (2000).
[32] S. T. Larsen and R. Taboryski, Langmuir **25**, 1282 (2009).
[33] T. Cubaud and M. Fermigier, J. Colloid Interface Sci. **269**, 171 (2004).
[34] M. K. Chaudhury and G. M. Whitesides, Science **256**, 1539 (1992).
[35] K. Ichimura, S. Oh, and M. Nakagawa, Science **288**, 1624 (2000).
[36] H. Gau, S. Herminghaus, P. Lenz, and R. Lipowsky, Science **283**, 46 (1999).
[37] J. Lèopoldés and D. G. Bucknall, J. Phys. Chem. B **109**, 8973 (2005).
[38] O. Bliznyuk, E. Vereshchagina, E. S. Kooij, and B. Poelsema, Phys. Rev. E **79**, 041601 (2009).
[39] H. P. Greenspan, J. Fluid Mech. **84**, 125 (1978).
[40] C. Huh and L. E. Scriven, J. Colloid Interface Sci. **35**, 85 (1971).
[41] J. F. Joanny and P.-G. de Gennes, J. Chem. Phys. **81**, 552 (1984).
[42] F. Brochard, Langmuir **5**, 432 (1989).
[43] S. Moulinet, C. Guthmann, and E. Rolley, Eur. Phys. J. E **8**, 437 (2002).
[44] L. W. Schwartz and R. R. Eley, J. Colloid Interface Sci. **202**, 173 (1998).
[45] U. Thiele and E. Knobloch, New J. Phys. **8**, 313 (2006).

[46] J. J. Huang, C. Shu, and Y. T. Chew, J. Colloid Interface Sci. **328**, 124 (2008).
[47] H. Kusamaataja and J. M. Yeomans, Langmuir **23**, 6019 (2007).
[48] L. M. Hocking, Q. J. Mech. Appl. Math. **34**, 37 (1981).
[49] L. M. Hocking, Q. J. Mech. Appl. Math. **36**, 55 (1983).
[50] K. Glasner, J. Comput. Phys. **207**, 529 (2005).
[51] C. Neto, D. R. Evans, E. Bonaccurso, H.-J. Butt, and V. S. J. Craig, Rep. Prog. Phys. **68**, 2859 (2005).
[52] C. I. Bouzigues, P. Tabeling, and L. Bocquet, Phys. Rev. Lett. **101**, 114503 (2008).
[53] P. Tabeling, Phys. Fluids **22**, 021302 (2010).
[54] M. A. Spaid and G. M. Homsy, Phys. Fluids **8**, 460 (1996).
[55] L. M. Pismen and J. Eggers, Phys. Rev. E **78**, 056304 (2008).
[56] N. Savva and S. Kalliadasis, Europhys. Lett. **94**, 64004 (2011).
[57] A. Münch, B. Wagner, and T. Witelski, J. Eng. Math. **53**, 359 (2005).